Effects of partial La filling and Sb vacancy defects on $CoSb_3$ skutterudites

Chongze Hu,[1,2] Xiaoyu Zeng,[3] Yufei Liu,[3] Menghan Zhou,[3] Huijuan Zhao,[1] Terry M. Tritt,[3] Jian He,[3,*] Jacek Jakowski,[4] Paul R. C. Kent,[4] Jingsong Huang,[4,*] and Bobby G. Sumpter[4]

[1]*Department of Mechanical Engineering, Clemson University, 201 Fluor Daniel EIB, Clemson, South Carolina 29634, USA*

[2]*Department of Mechanical Engineering, University of Minnesota-Twin Cities, 111 Church Street SE, Minneapolis, Minnesota 55455, USA*

[3]*Department of Physics & Astronomy, Clemson University, 118 Kinard Laboratory, Clemson, South Carolina 29634, USA*

[4]*Center for Nanophase Materials Sciences and Computational Sciences & Engineering Division, Oak Ridge National Laboratory, Bethel Valley Road, Oak Ridge, Tennessee 37831, USA*

(Received 3 March 2017; published 25 April 2017)

Over the past decade, the open frame ("cagey") structure of $CoSb_3$ skutterudite has invited intensive filling studies with various rare-earth elements for delivering state-of-the-art midtemperature thermoelectric performance. To rationalize previously reported experimental results and provide new insight into the underexplored roles of La fillers and Sb vacancies, *ab initio* density functional theory studies, along with semiclassical Boltzmann transport theory calculations, are performed for pristine $CoSb_3$ of different lattice settings and La-filled $CoSb_3$ with and without Sb's mono- and divacancy defects. The effects of spin-orbit coupling (SOC), partial La filling, Sb vacancy defects, and spin polarization on the electronic and thermoelectric properties are systematically examined. The SOC shows minor effects on the electronic and thermoelectric properties of $CoSb_3$. The peculiar quasi-Dirac band in the pristine $CoSb_3$ largely survives La filling but not Sb vacancies, which instead introduce dispersive bands in the band gap region. The non-spin-polarized and spin-polarized solutions of La-filled $CoSb_3$ are nearly degenerate. Importantly, the band structure, density of states, and Fermi surface of the latter are significantly spin polarized, giving rise to spin-dependent thermoelectric properties. Seebeck coefficients directly calculated as a function of chemical potential are interpreted in connection with the electronic structures. Temperature-dependent Seebeck coefficients derived for the experimentally studied materials agree well with available experimental data. Seebeck coefficients obtained as a function of charge carrier concentration corroborate the thermoelectrically favorable role at high filling fractions played by the Fermi electron pockets associated with the degenerate valleys in the conduction bands, and also point toward a similar role of the Fermi hole pockets associated with the degenerate hills in the valence bands. These results serve to advance the understanding of $CoSb_3$ skutterudite, a class of materials with important fundamental and application implications for thermoelectrics and spintronics.

DOI: 10.1103/PhysRevB.95.165204

I. INTRODUCTION

To date the worldwide appetite for sustainable energy remains a grand challenge that motivates intensive research on various energy conversion technologies [1]. Thermoelectric materials, which can convert temperature differences into electric voltage and vice versa, play an important role in the energy conversion field [2]. Skutterudites with a general formula of MX_3 (M = Co, Rh, or Ir; X = P, As, or Sb) and a space group of $Im\bar{3}$ (no. 204) establish a class of promising thermoelectric materials, as a result of their open frame ("cagey") structures [3,4]. Taking $CoSb_3$, for example, the crystal structure of skutterudites is characterized by a body-centered cubic (bcc) unit cell with a network of corner-sharing octahedra, each of which consists of one Co center and six Sb vertices [Fig. 1(a)] [4]. Lying at the center of the bcc cell is a nanosized dodecahedron cage enclosed by eight Co atoms and six pairs of Sb atoms where a guest filler atom can be filled in [Fig. 1(b)]. Alternatively, the structure can also be viewed as a simple cubic sublattice of Co atoms by shifting the unit cell shown in Fig. 1(a) by $\frac{1}{2}$ lattice along the body diagonal [4], giving a new unit cell consisting of eight Co cubes, six of which are occupied by a Sb_4 ring while two remain vacant. In fact, Fig. 1(b) shows such a Co cube free of Sb_4 ring but filled by a guest atom. These skutterudites have motivated work on filling the cages with diverse atoms in conjunction with the routine substitutional doping efforts to tailor specific functions and applications. Extensive studies in this vein have revealed a variety of interesting physical properties ranging from metal-to-insulator transitions [5,6], magnetic ordering [7,8], unconventional superconductivity [9,10], heavy fermion state [10,11], and non-Fermi-liquid behaviors [12,13] to valence fluctuations or Kondo behaviors [14,15].

Among the skutterudite family, $CoSb_3$ is specifically named as Kieftite after Cornelis Keift in the mineralogical community [16]. It is featured by high carrier mobility and high lattice thermal conductivity, both of which are attributed to the covalent nature of chemical bonding. While the high mobility is thermoelectrically favorable, the high lattice thermal conductivity is not. To improve the performance of $CoSb_3$ toward state-of-the-art midtemperature thermoelectric materials, extensive experimental and theoretical investigations have focused on filling the naturally formed nanosized cages with alkali metals, alkaline earth metals, or rare earth filler atoms [17–21], or doping at the Co and/or Sb sites [22,23], or implementing both measures simultaneously [24–29]. In the context of a phonon-glass electron-crystal paradigm [3,30], the filler atoms rattle in the cage and strongly scatter the

*Corresponding authors: jianhe@g.clemson.edu; huangj3@ornl.gov

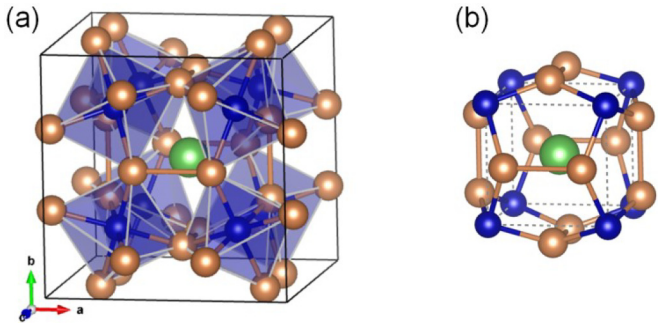

FIG. 1. Simple cubic view of the body-centered cubic crystal structure of $CoSb_3$ skutterudite with a network of corner-sharing octahedra (a) and with a guest atom filled into the dodecahedron cage (b). The dashed lines in (b) illustrate the Co cube. Transition metals, pnictogens, and the filler atom are shown in blue, yellow, and green, respectively.

heat-carrying phonons towards a phonon-glass behavior [31], while the dopants optimize the electronic band structure towards an electron-crystal behavior [32]. A complication to the thermoelectric material research comes from the often unavoidable vacancies in the materials, e.g., by losing Sb atoms due to evaporation or forming a secondary phase with the filler elements during material synthesis [33]. However, the role of vacancies is underexplored, let alone the interplay between the fillers and vacancies.

La is a unique filler atom to study in the sense that it is the lightest lanthanide element and the only one without f electrons compared with other studied rare earth filler atoms such as Ce [34,35], Pr [36], Eu [37], and Yb [38–40]. The studies on La filling may shed light on the role of f electrons in filling and rattling when compared with studies on other elements. From a practical standpoint, a multiple filling approach [41,42] turns out to be more effective than single La filling [43,44] in enhancing the midtemperature thermoelectric performance. However, the effect of La filling is entangled with other effects in multiple fillings. Therefore, single La filling studies merit further scrutiny despite the fact that their performances are unfavorable and relevant reports are scarce. Table I summarizes the filling fraction, Sb vacancy, lattice constant, conductivity type, and carrier concentration from a limited number of experimental studies on La-filled $CoSb_3$ [43–45]. For simplicity, a few experimental studies on La-filled $CoSb_3$ with simultaneous doping at the Co or Sb sites are excluded [24,29,32]. Note that all of the experimental samples have a partial La filling that is lower than the experimental filling fraction limit (FFL) of 23% found by Nolas *et al.* [45]. Interestingly, this FFL is accompanied by a small degree of Sb vacancy. Theoretical FFL for La predicted by Shi *et al.* based on density functional theory (DFT) is slightly lower at 21% [46]. The partial fillings of Park *et al.* reached as high as 40% [43]. However, it is a nominal filling fraction based on the starting mixture for synthesis, whereas the actual filling fraction could be lower, as shown by Mi *et al.* [44,47]. It can also be seen from the table that La filling tends to slightly expand the lattices even though it is filled into the void. Additionally, $CoSb_3$ without La filling is typically P-type with carrier concentrations p on the order of 10^{18} cm^{-3}. With La filling, $CoSb_3$ is converted to N-type with carrier concentrations n on the order of 10^{20} cm^{-3}. For the sample with Sb vacancies, the carrier concentration is further increased to the order of 10^{21} cm^{-3}.

Motivated by these experimental works, herein we perform theoretical studies of La-filled $CoSb_3$ with and without Sb's vacancy defects, to rationalize the experimental results and provide insight into the underexplored roles of La fillers and Sb vacancies. Early theoretical studies adopted a 100% filling fraction for computational convenience [48]. Zhou *et al.* [49] carried out calculations for a reasonable La filling fraction of 12.5%, but without including spin polarization. Although not important for unfilled systems, spin polarization could be indispensable for filled skutterudites. In addition, no Sb vacancy has been taken into account in previous theoretical studies. Therefore, in this work, we apply *ab initio* DFT in combination with semiclassical Boltzmann transport theory to study partial La-filling and Sb vacancy defects, along with other effects such as spin-orbit coupling and spin polarization, with an aim to establish a causal relationship between electronic structures and thermoelectric properties. The paper is organized as follows. In Sec. II, we summarize the skutterudite structures of this study and the computational methodology. In Sec. III, we present the results and discussion.

TABLE I. Experimentally studied $La_xCo_4Sb_{12-y}$ skutterudites with different amount of La filling fraction (FF) x and Sb vacancy defects y. Carrier concentration ρ is p and n for P-type and N-type materials, respectively.

Formula	x				Conductivity	Carrier concn.	Thermoelectric	
$La_xCo_4Sb_{12-y}$	Nominal	Actual	y	a (Å)	type	ρ (10^{18} cm^{-3})	T range (K)	Refs.
Co_4Sb_{12}	0	0	0	9.032(11)[a]	P	1.88[b]	6–300	[45]
Co_4Sb_{12}	0	0	0		P	2.57[c]	323–823	[43]
$La_{0.05}Co_4Sb_{12}$		0.05	0	9.056(17)[a]	N	170[b]	6–300	[45]
$La_{0.1}Co_4Sb_{12}$	0.1	0.049	0	9.0427(1)[a]	N	105–230[d]	2–380	[44]
$La_{0.1-0.4}Co_4Sb_{12}$	0.1–0.4		0		N	127–368[c,e]	323–823	[43]
$La_{0.23}Co_4Sb_{11.6}$		0.23	0.4	9.060(13)[a]	N	2010[a]	6–300	[45]

[a]300 K characterizations.
[b]Only the 300 K p or n values reported.
[c]Only the room-temperature p or n values reported.
[d]Temperature dependent n reported in the range 2–300 K.
[e]Filling fraction x dependent n values.

Our approach is to first revisit $CoSb_3$'s electronic structures of different lattice settings, and then move forward to the electronic structures of partially La-filled $CoSb_3$, first without and then with mono- and divacancy defects. Next we examine the Seebeck coefficient that lies at the heart of thermoelectric properties. In Sec. IV, we conclude with a summary of the main findings of this work.

II. METHODOLOGY

Three types of skutterudite structures were calculated, including (i) pristine $CoSb_3$, (ii) La-filled $CoSb_3$, and (iii) La-filled $CoSb_3$ with mono- or divacancy defects. For pristine $CoSb_3$, the simple cubic cell (Co_8Sb_{24}) was used to test theories for structural optimizations, while the bcc primitive cell (Co_4Sb_{12}) and the bcc $2 \times 2 \times 2$ supercell ($Co_{32}Sb_{96}$) were used to calculate the electronic structures. The bcc supercell contains eight dodecahedron voids, each enclosed by eight Co atoms and six pairs of Sb atoms. The structure of La-filled $CoSb_3$ was constructed by filling one of the eight voids in the bcc supercell, giving $LaCo_{32}Sb_{96}$, or equivalently $La_{0.125}Co_4Sb_{12}$, with a filling fraction of 12.5%. The structures of La-filled $CoSb_3$ with a monovacancy defect were constructed by removing one Sb atom at six random positions while those with a divacancy defect were created by removing a directly bonded Sb pair at six random positions, yielding $LaCo_{32}Sb_{95}$ or equivalently $La_{0.125}Co_4Sb_{11.875}$, and $LaCo_{32}Sb_{94}$ or equivalently $La_{0.125}Co_4Sb_{11.750}$, respectively. For the structural optimizations of the simple cubic cell, the bcc primitive cell, the bcc supercell of $CoSb_3$, and the La-filled $CoSb_3$, both the lattice constant and atomic positions were relaxed. For the La-filled $CoSb_3$ with vacancy defects, only atomic positions were relaxed while the lattice constant from the optimized La-filled $CoSb_3$ was kept constant.

DFT calculations were performed with the Vienna *ab initio* simulation package (VASP, version 5.3.3) [50,51]. The Kohn-Sham equations were solved with the projector-augmented wave (PAW) method [52,53]. A gamut of exchange-correlation functionals with and without van der Waals (vdW) corrections was tested for structural optimizations. It has been previously shown that vdW interactions can alter the structural and cohesive properties not only for layered materials [54,55], but also for three-dimensional (3D) bulk materials including ionic solids [56,57]. On the basis of the tests (Tables S1 and S2, Supplemental Material [58]), a nonlocal optB86b-vdW functional [59] was adopted for the structural optimizations, where all atoms were relaxed until the Hellmann-Feynman forces were smaller than 10^{-2} eV/Å. Following the structural optimizations, static electronic structures were calculated using the semilocal Perdew-Burke-Ernzerhof (PBE) exchange-correlation functional [60]. The Brillouin-zone integrations were performed on Γ-centered $8 \times 8 \times 8$ and $4 \times 4 \times 4$ k-point grids for the primitive and supercells, respectively, the kinetic energy cutoff for plane waves was set to 500 eV, the convergence criterion for electronic self-consistency was set to 10^{-5} eV, and the "accurate" precision setting was adopted to avoid wrap around errors. Band structures were sampled in reciprocal space using primitive-based high symmetry k-points Γ (0, 0, 0), H (0.5, −0.5, 0.5), N (0, 0, 0.5), and P (0.25, 0.25, 0.25).

Spin-orbit coupling (SOC) effects were investigated for the bcc primitive lattice of the pristine Co_4Sb_{12}. The results indicate that the SOC effects on band structures are insignificant, in agreement with the expectation from a previous study [61]. SOC calculations could not be computationally afforded for the La-filled systems with and without vacancy defects due to the large size of the supercells. However, SOC calculations for other $LaRu_4X_{12}$ (X = P, As, Sb) skutterudites indicate no pronounced SOC effect in the vicinity of the Fermi energy [62], implying that the SOC effects are negligible for the La-filled systems under the present studies. For band gap corrections, a scissor operator Δ was applied to the PBE-based electronic structure by shifting up the conduction bands without changing the valence bands. The amount of correction was based on a many-body quasiparticle GW result in the literature (see details below). Non-spin-polarized calculations were performed for the systems without La filling while spin polarization was turned on for the La-filled systems. Fermi surfaces were calculated by using the Wannier90 program [63], and then visualized with the XCrysDen program [64].

Thermoelectric Seebeck coefficients $S(\mu,T)$ were calculated on a grid of chemical potential μ and temperature T by using the BoltzWann program [65]. The relaxation time was set to a constant value of 10 fs [65]. A dense mesh $100 \times 100 \times 100$ for band interpolation and a small energy bin width of 10^{-3} eV were adopted in the calculations. Seebeck coefficients $S(\mu,T)$ were first calculated for Co_4Sb_{12}, $La_{0.125}Co_4Sb_{12}$, $La_{0.125}Co_4Sb_{11.875}$, and $La_{0.125}Co_4Sb_{11.750}$. To obtain Seebeck coefficients as a function of T for $La_{0.125}Co_4Sb_{12}$, we integrated the total number of electrons $n_e = \int f(E)g(E)dE$ for each temperature T, where $f(E)$ is the Fermi-Dirac (FD) distribution function and $g(E)$ is its density of states (DOS), in order to find the chemical potential $\mu(T)$ that gives the correct n_e. Using the chemical potential $\mu(T)$, we interpolated the $S(\mu,T)$ values from the grid of μ and T to obtain the $S(T)$. To facilitate the comparison between theoretical calculations and the experimental $S(T)$ of P-type Co_4Sb_{12}, and N-type $La_{0.05}Co_4Sb_{12}$, $La_{0.1}Co_4Sb_{12}$, and $La_{0.23}Co_4Sb_{11.6}$ [44,45], the integration was based on the DOS of the pristine Co_4Sb_{12} to find the chemical potential $\mu(T)$ that yields the experimental carrier concentrations. Seebeck coefficients as a function of carrier concentrations for generic P- and N-type Co_4Sb_{12} were obtained in a similar way. Only majority carriers were considered while the effect of minority carriers was neglected [65].

III. RESULTS AND DISCUSSION

A. Electronic structures of bcc primitive cell (Co_4Sb_{12})

We start by revisiting the electronic structures of the well-studied $1 \times 1 \times 1$ bcc primitive cell (Co_4Sb_{12}). The structure was first optimized with the nonlocal optB86b-vdW functional. The static electronic structure was then calculated with the PBE functional. The band structure, total DOS, and Fermi surface are shown in Fig. 2. As can be seen from the band structure [Fig. 2(a)], a direct band gap of 0.23 eV exists at the Γ point between the valence band maximum (VBM) and the conduction band minimum (CBM). This value is the same as the LDA result of Wee *et al.* [66], comparable to the LDA and PBE results of 0.22 and 0.17 eV calculated by Sofo

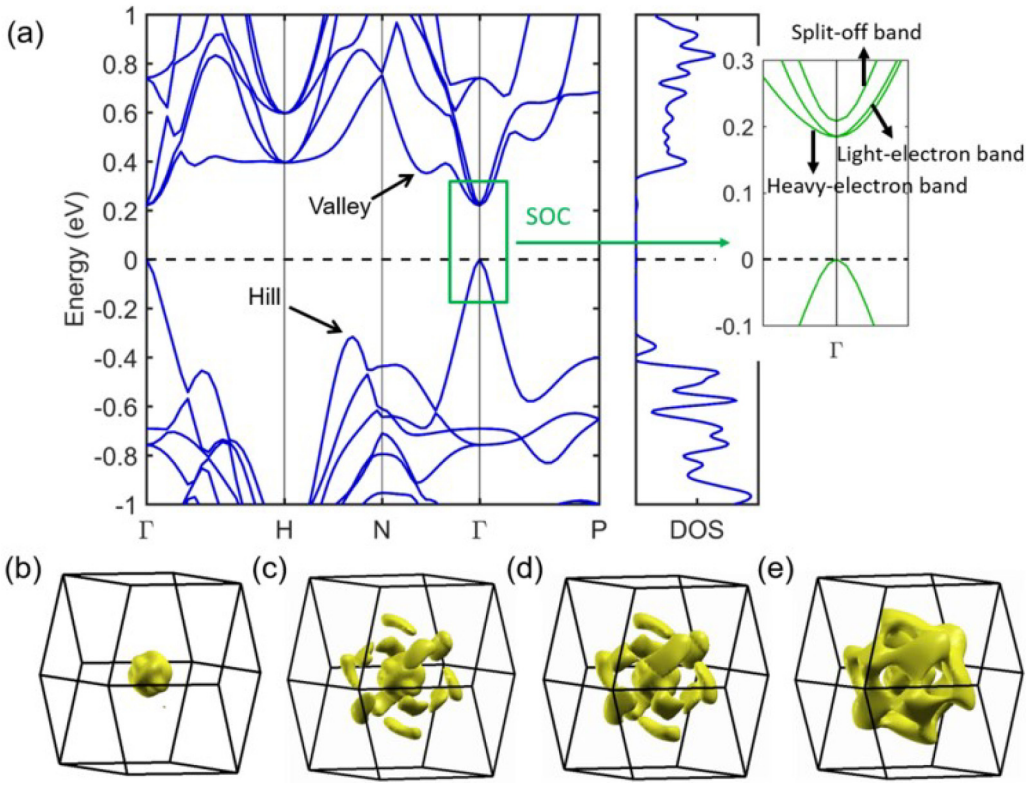

FIG. 2. (a) Band structure and total density of states (DOS) for the $1 \times 1 \times 1$ body-centered cubic (bcc) primitive cell (Co_4Sb_{12}), showing a valley band located at 0.13 eV above the conduction band minimum (CBM) and a hill band located at 0.32 eV below the valence band maximum (VBM). The Fermi energy, denoted by the horizontal dashed line, is set to 0 eV at the top of the valence bands. The inset shows the band structure around the zone center calculated with inclusion of spin-orbit coupling (SOC) effect. (b)–(e) The Fermi surface at different energy levels, from 0.13, 0.14, 0.15, to 0.16 eV above the CBM.

and Mahan [67], and also within the LDA range of 0.195–0.330 eV calculated by Lefebvre-Devos *et al.* [68]. Unlike the band structure, the DOS shows an indirect pseudogap of 0.57 eV between the first peak of valence DOS located at −0.34 eV below the VBM and the tiny conduction DOS peak corresponding to the CBM. In comparison, the direct gap identified from the band structure is hardly discernable from the DOS since the peak corresponding to the VBM at the Γ point is too low. This pseudogap value is the same as the theoretical result of Singh and Pickett [61]. Singh and Pickett further identified a direct pseudogap of 0.80 eV at the Γ point by neglecting the single valence band that makes little DOS contributions [61]. In our calculations, this direct pseudogap is only slightly larger.

The theoretical predictions of band gaps for $CoSb_3$ turn out to be a complicated and challenging problem. Hammerschmidt *et al.* conducted a systematic study of $CoSb_3$'s lattice and electronic structure using various exchange-correlation functionals and found a wide range of band gap values from 0.1 to 4.5 eV depending on the methods applied [69]. The different functionals affect the band gap indirectly by changing the lattice constant and directly by the amount of Hartree-Fock exchange included. It is known that DFT tends to underestimate the band gap for semiconductors and insulators, whereas the mixing of Hartree-Fock exchange may give larger band gaps. Further, Kahn *et al.* calculated the band gaps of a series of skutterudites with a many-body quasiparticle GW approach and obtained a band gap value of 0.34 eV for $CoSb_3$ [70]. They also examined the band gaps using regular and nonregular Tran and Blaha modified Becke-Johnson (TB-mBJ) methods [71,72], and concluded that the generally reliable GW method underestimated the band gaps and instead the nonregular TB-mBJ method reproduced the experimental band gaps, due to the large spread of charge densities in the nanosized cage of skutterudite structures. However, their comparisons were made between experimental optical band gaps, very likely vertical transitions without momentum transfer, and the smallest theoretical band gaps, which were transformed from direct into indirect band gaps by the TB-mBJ methods.

Experimental band gap measurements and interpretations are equally complicated and challenging. A broad range of experimental band gap values have been reported from ≥0.5 eV [23,73–75], to intermediate 0.31–0.35 eV [76,77], and further down to very small 0.03–0.05 eV [77–79]. The wide range of band gap values can be attributed to the possibility that the experimental values measured by different methods may correspond to one of the three theoretically identified band gaps including the direct pseudogap, the indirect pseudogap, and the direct gap. For instance, the largest optical gap may need to be compared with the direct pseudogap at the Γ point [61], while the experimental band gaps of 0.6–0.7 eV measured by transport property and Hall probe measurements [23,73,74] may need to be compared with the

indirect pseudogap [23,74]. The experimental estimation of 0.5 eV via the high temperature electrical resistivity measurement [75] could be compared with the indirect pseudogap as well [61]. Further, Mandrus *et al.* obtained an intermediate band gap of 0.31 eV in the temperature range of >400 K and a small band gap of 0.05 eV between 130 K and 400 K by resistivity measurements [77]. They compared the intermediate gap of 0.31 eV with the experimental value of 0.5 eV [75], which however was assigned to the indirect pseudogap [61]. It is possible that this intermediate band gap value corresponds better with the theoretical direct band gap. Finally, possible contributions from impurities to the smallest band gap values cannot be ruled out. We note that the comparisons summarized here are not unambiguous without backing from further calculations using hybrid DFT, or many-body quasiparticle GW, or even GW plus the Bethe-Salpeter equation. Nevertheless, these complications on both the theoretical and experimental sides indicate the necessity to differentiate between direct pseudogaps, indirect pseudogaps, direct band gaps, and impurity-induced band gaps.

Singh and Pickett uncovered a remarkable feature in the band structure of pristine skutterudite, i.e., a single valence band crossing the pseudogap shows largely a quasilinear dispersion, except for a quadratic shape in a narrow region near the zone center [61]. Recently, Smith *et al.* put forth a theoretical model showing that this quasilinear pseudogap-crossing band is associated with the massless Dirac bands [80] that is similar to the case of graphene [81] and recently discovered 3D Dirac-Weyl semimetals [82–84]. By varying the Sb atomic coordinates, they revealed a critical point along the transformation path from perovskite toward skutterudite where the two massless Dirac bands touch each other and meanwhile become degenerate with two other massive conduction bands. Accordingly, the Fermi surface appears as just a topological point at the zone center. Simply by a small structural deviation from the critical point, the fourfold degeneracy is lifted yielding a small direct band gap at the Γ point. Since the mineral skutterudite is naturally very near the critical point, the direct gap of skutterudite turns out to be small and highly sensitive to the atomic positions of antimony [66,67]. Such sensitivity was previously ascribed to the antibonding π_4 orbital feature of the Sb_4 ring at the VBM [67]. However, the Sb_4 rings were later found not to be the main structural feature to analyze the highest valence band behavior [68].

It can be seen in Fig. 2(a) that the quasilinear valence band symmetrically flanks the Γ point and features a large dispersion. Calculations give a slope of +3.03 and −3.02 eV Å in the Γ-N and Γ-P zone, respectively. Three conduction bands above the quasilinear valence band are triply degenerate at the Γ point. Along the Γ-N direction, they diverge immediately into three separate bands; however, along the Γ-P direction, they separate into a pair of doubly degenerate bands of lower energy and a single band of higher energy. It is worth noting that, unlike the two lower-energy massive bands that are quadratic in shape, the third higher-energy conduction band mirrors the pseudogap-crossing valence band in relation to the massless Dirac band. Calculations give a slope of −3.03 and +2.96 eV Å in the Γ-N and Γ-P zone, respectively, which is close to that of its valence counterpart. By turning on SOC for the bcc primitive cell Co_4Sb_{12}, the degeneracy is lifted for the three conduction bands except at the Γ point for the two lower bands [cf. the inset of Fig. 2(a)]. The two lower conduction bands are a heavy-electron band and a light-electron band, respectively, while the third is a split-off band lying only 0.02 eV above at the Γ point, which remains quasilinear even with SOC. In the meantime, the direct band gap at the Γ point is reduced only slightly to 0.18 eV. In light of small SOC effects for pristine Co_4Sb_{12} shown herein and for compositionally similar $LaRu_4X_{12}$ (X = P, As, Sb) skutterudites reported in the literature [62], SOC is not applied toward the electronic structure calculations of the La-filled systems to be discussed below.

Another notable feature of the band structure [cf. Fig. 2(a)] is the valley band in the Γ-N zone. It is one of twelve degenerate valleys in the entire Brillouin zone as dictated by the rhombic dodecahedron shape for the Brillouin zone with twelve congruent rhombic faces. Figure 2(a) shows that the bottom of the valley band is located at 0.13 eV above the CBM, agreeing with the result of Tang *et al.* within 0.02 eV [85]. The small discrepancy may be caused by the norm-conserving pseudopotentials used in their calculations as compared to the PAW potentials applied in this work. Note that the Fermi energy for the pristine system should be located within the gap; however, the extra electrons brought to the host matrix by *N*-type doping such as La filling may raise the Fermi energy above the valley bottom. Recently, Tang *et al.* pointed out that the valley bottom represents the starting point to form twelve isolated Fermi pockets [85]. Due to the high effective mass of electrons at these degenerate valleys, the related Fermi pockets account for the high thermoelectric power factor at high doping ratios [86]. Figures 2(b)–2(e) show the topological variation of the Fermi surface by manually shifting up the Fermi energy. First the Fermi surface is only a core pocket, which consists of three shells of isoenergy surface corresponding to the three lowest conduction bands (the inner two shells are invisible). Above the valley bottom, twelve peripheral pockets start to appear around the core pocket. They increase in size with increasing Fermi energy and eventually coalesce together with the core pocket once the Fermi energy is raised above the maximum between the valley and the CBM. Fermi surfaces for other systems studied below will be compared with these results.

Notably, there is also a hill band in the H-N zone of the band structure [Fig. 2(a)], which corresponds to the starting point for the first peak of valence DOS located at −0.34 eV below the VBM. Similar to its valley counterpart discussed above, this hill band should also be highly degenerate due to the twelve congruent faces of the rhombic-dodecahedron-shaped Brillouin zone. Although the Fermi energy for the pristine system is located within the gap, the extra holes brought to the host matrix by *P*-type doping may serve to lower the Fermi energy below the hill top. Unlike the valley bottom that is located only at 0.13 eV above the CBM, the hill top is a lot lower than the VBM. Nonetheless, the Fermi energy can still be lowered below the hill top, due to the small DOS of quasi-Dirac valence bands. The hill top represents the starting point to form degenerate Fermi pockets (not shown), which belong to hole pockets instead of electron pockets due to *P*-type doping. Again, due to the high effective mass of holes at the degenerate

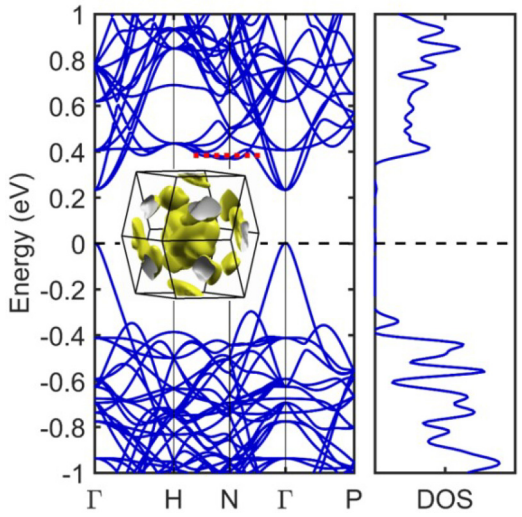

FIG. 3. Band structure and total density of states (DOS) for the body-centered cubic (bcc) $2 \times 2 \times 2$ supercell ($Co_{32}Sb_{96}$). The Fermi energy, denoted by the horizontal dashed line, is set to 0 eV at the top of the valence bands. The inset shows the Fermi surface at 0.14 eV above the CBM as indicated by the red dashed line.

hills, these hole pockets could be thermoelectrically favorable at high doping ratios.

B. Electronic structures of bcc supercell ($Co_{32}Sb_{96}$)

Next we examine the bcc $2 \times 2 \times 2$ supercell ($Co_{32}Sb_{96}$) that contains eight dodecahedron voids, in order to compare with the bcc primitive cell shown above and the $LaCo_{32}Sb_{96}$ (or equivalently $La_{0.125}Co_4Sb_{12}$) system to be discussed below. The bcc supercell structure was first optimized with the nonlocal optB86b-vdW functional, and then the static electronic structure was calculated with the PBE functional. As expected, the optimized lattice structure of the bcc supercell is commensurate with that of the bcc primitive cell. The electronic structures including band structure, total DOS, and Fermi surface are presented in Fig. 3. Our results are comparable to the previous results of Tang *et al.* calculated for the same bcc $2 \times 2 \times 2$ supercell [87]. Compared to the bcc primitive cell, the doubling of lattices in all three vector directions gives a bcc $2 \times 2 \times 2$ supercell that is $8 \times$ as large in the direct space and a Brillouin zone that is $1/8 \times$ as small in the reciprocal space. Consequently, the bands of the supercell show intricate backfolding compared to the primitive cell. Nevertheless, the gap-crossing quasi-Dirac band is still clearly visible. The valley band located in the middle of Γ-N zone in the bcc primitive cell [Fig. 2(a)] is now shifted closer to the N point and becomes nearly doubly degenerate (Fig. 3). In addition, the hill band in the H-N zone [Fig. 2(a)] is now shifted into the Γ-N zone (Fig. 3). However, these changes do not alter the band gap values or the DOS features.

The inset of Fig. 3 shows the Fermi surface for the bcc supercell located at 0.14 eV above the CBM as indicated by the red dashed line. Again, the Fermi energy for the unfilled system should be located within the gap, but as will be shown below for the La-filled system, the extra electrons introduced by La filling will raise the Fermi energy above the valley bottom. The Fermi surface thus features a core pocket in the center of the Brillouin zone and twelve degenerate half pockets surrounding the core. The core pocket resembles that of the bcc primitive cell shown in Figs. 2(b)–2(d). However, the twelve peripheral pockets in the case of bcc $2 \times 2 \times 2$ supercell are truncated by the zone boundary due to the $1/8 \times$ smaller Brillouin zone. Apparently, the band structures and Fermi surfaces of the bcc supercell are different from those of the bcc primitive cell presented above. However, these differences only arise from the different lattice settings used for the calculations, and do not indicate different electronic properties. Indeed, the total DOS is essentially the same after normalization by the number of atoms. Therefore, transport properties including Seebeck coefficients calculated based on the electronic structure of the bcc supercell should be identical to those calculated based on the bcc primitive cell.

C. $La_{0.125}Co_4Sb_{12}$ without Sb vacancies

With the electronic structures for the parent skutterudite well understood, we turn to the $La_{0.125}Co_4Sb_{12}$ structure that has a filling fraction of 12.5%. Earlier theoretical calculations considered stoichiometric $LaCo_4Sb_{12}$ with a full La filling [48]. However, as Singh pointed out, the actual as-measured material is likely La deficient [88]. The filling fraction limit for La in $CoSb_3$ was theoretically predicted to be ∼21% [46]. A La filling fraction of 5%–23% has also been studied experimentally where the 23% La filling is accompanied by Sb defects in $La_{0.23}Co_4Sb_{11.6}$ [44,45,47]. Interestingly, a stoichiometric $\beta - LaCoSb_3$ has been prepared by solid-state reactions and characterized by x-ray diffraction showing that it has an orthorhombic lattice [89]. As a result of the high La component, its structure is drastically different from skutterudite by the presence of alternatively stacked layers of Sb square nets with a small distortion and La-covered $CoSb_2$ slabs featuring Co-Co dimers. Herein we study only the $La_{0.125}Co_4Sb_{12}$ system that adopts the skutterudite structure.

By using the nonlocal optB86b-vdW functional, the non-spin-polarized and spin-polarized calculations gave two different solutions: the spin-polarized solution is more stable than the non-spin-polarized solution by 2 meV per unit cell (Table S3, Supplemental Material [58]). However, convergence studies under stringent conditions gave a very small energy difference of ∼0.5 meV per unit cell, indicating that the two solutions are nearly degenerate (Table S4, Supplemental Material [58]). The lattice constant for the bcc supercell of $La_{0.125}Co_4Sb_{12}$ was optimized to be 9.080 and 9.083 Å with and without spin polarization, slightly larger than the theoretical value of 9.066 Å for Co_4Sb_{12} without La filling. The small expansion of lattice constant is due to the cage filling [34]. These results agree well with the room-temperature experimental values of 9.032 Å without and 9.043 Å with La-filling [44,45,47]. From the structural optimizations, the La filler atom is found to be located exactly at the center of the dodecahedron cage. However, Mi *et al.* found via fitting experimental atomic displacement parameters (ADPs) with an Einstein model that La was slightly displaced by 0.06 Å from the cage center, which was ascribed to

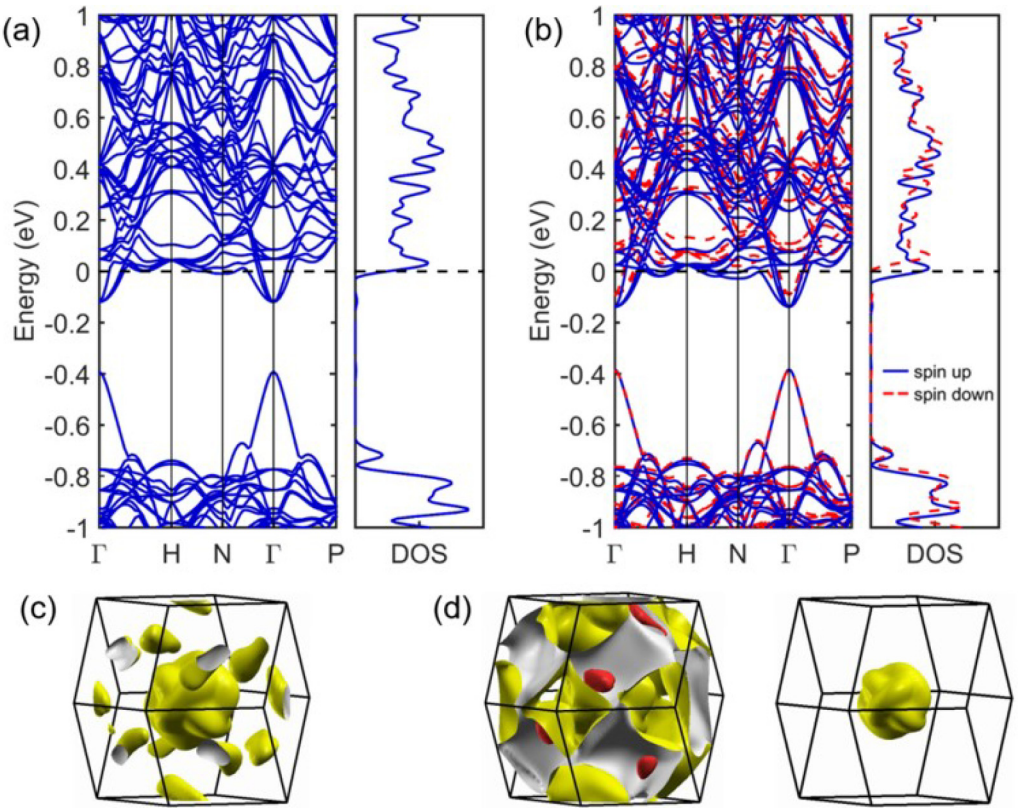

FIG. 4. Band structures and total density of states (DOS) for $LaCo_{32}Sb_{96}$ (or $La_{0.125}Co_4Sb_{12}$) without spin polarization (a) and with spin polarization (b), and their respective Fermi surfaces (c) and (d). With spin polarization (d), the Fermi surface is shown for the spin-up electron (left) and the spin-down electron (right), respectively. The spin-up Fermi surface shows two layers of peripheral pockets, with the inner layer shown in red. The horizontal dashed line denotes the Fermi energy.

a possible covalent bonding with the host matrix. Starting from the optimized structure of $La_{0.125}Co_4Sb_{12}$, we carried out further rigid scans of potential energy surfaces (PESs) by displacing the La atom from the cage center along five representative paths. All of the PESs indicate that the potential energy minimum is located at the cage center without La displacements (Fig. S1, Supplemental Material [58]). Our results imply that the small displacement of the La filler atom found by Mi *et al.* may have originated from small structural disorders.

The optimized crystal structures of $La_{0.125}Co_4Sb_{12}$ were subjected to static band structure calculations with the PBE functional. Figure 4(a) shows the band structure and total DOS calculated by non-spin-polarized DFT, while Fig. 4(b) shows the spin-polarized counterparts. As shown in Fig. 4(a), the non-spin-polarized band structure and DOS of $La_{0.125}Co_4Sb_{12}$ bear a large degree of similarity to the electronic structures of its parent structure except for the shifted up Fermi energy (cf. Fig. 3) and a slight increase of the direct band gap induced by the extra electrons donated from the filler to the host matrix [66]. This similarity indicates that the bands of the parent structure are rigid, allowing the quasi-Dirac band to survive the partial La filling. As expected based on the electronic structures of the bcc primitive cell and supercell shown above, the low La filling fraction largely serves to raise the Fermi energy to a position slightly above the bottom of the valley bands. This observation is consistent with the report by Zhou *et al.* that the band structures of $R_{0.125}Co_4Sb_{12}$ systems single-filled with nine kinds of atoms including La exhibit no significant changes compared with that of $CoSb_3$ [49].

Spin-polarized calculations for $CoSb_3$ skutterudite have been reported for its surface properties [90], but are rarely applied to investigate the role of filler atoms in $CoSb_3$. As can be seen from Fig. 4(b), the two spin channels display a large band offset for the conduction bands. Following the terminologies used for the pristine $CoSb_3$ without La filling, the CBM at the Γ point for the spin-down channel is raised with respect to that for the spin-up channel, while the VBMs for both spins are essentially the same. As a result, the direct band gap is larger for the spin-down channel than the spin-up counterpart. In addition, the Fermi energy is located at ∼0.14 eV above the CBM of the spin-up channel but is located at ∼0.09 eV above the CBM of the spin-down channel, compared to the location of 0.12 eV for the Fermi energy of the non-spin-polarized band structure. Spin-polarization effects can be also seen from the DOS curves. The Fermi energy for the spin-up channel is shifted up to nearly the top of the DOS peak at the expense of that for the spin-down channel. In comparison, the non-spin-polarized results in Fig. 4(a) show that the Fermi energy is located in the middle of the hillside. Further, as a result of the spin polarization, the spin magnetization of the system is 2.35 μ_B (Table S3, Supplemental Material [58]), in line with the large band offset between the two spin channels.

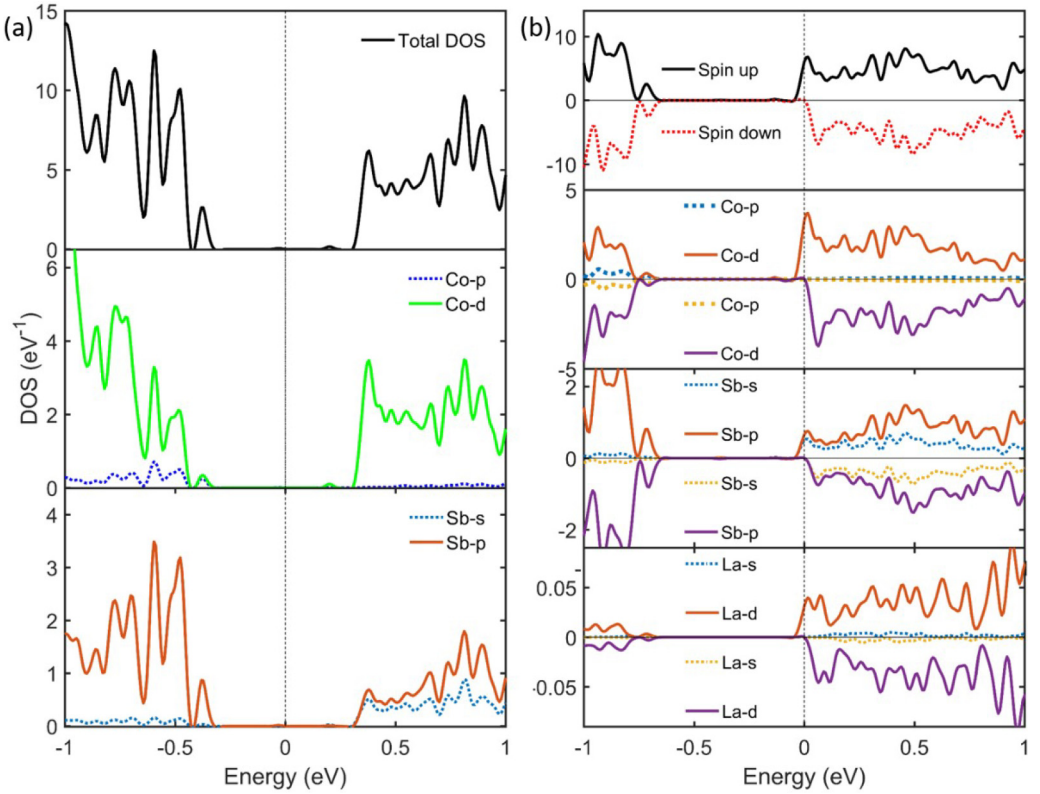

FIG. 5. Total and partial density of states (DOS) for the body-centered cubic (bcc) $2 \times 2 \times 2$ supercell ($Co_{32}Sb_{96}$) without spin polarization (a) and $LaCo_{32}Sb_{96}$ (or $La_{0.125}Co_4Sb_{12}$) with spin polarization (b). For the semiconducting $CoSb_3$, the Fermi energy, as indicated by the vertical dashed line, is set to 0 eV at the edge of the valence bands.

The Fermi surfaces in association with the degenerate valleys could be non-spin polarized or spin polarized, depending on the electronic structures. Figure 4(c) shows the non-spin-polarized Fermi surface of $La_{0.125}Co_4Sb_{12}$ at the calculated Fermi energy, which is very similar to the topology of the Fermi surface shown in Fig. 3. Note that with the La filling fraction of 12.5%, the number of extra electrons is only 0.375 when normalized to each bcc primitive cell, as compared to the 0.5 electrons per cell for $Yb_{0.25}Co_4Sb_{12}$ [85]. Such a small amount of extra electrons is barely enough to raise the Fermi energy above the valley bottom [Fig. 4(a)]. In comparison, the spin-polarized Fermi surfaces in Fig. 4(d) are dramatically different as a result of the large conduction band offset. Due to spin polarization, the Fermi energy for the spin-up channel is raised to be well above the valley bottom, while that for the spin-down counterpart is lowered below the degenerate valleys [Fig. 4(b)]. Consequently, the Fermi surface for the spin-up channel shows large peripheral open pockets joined together, while that for the spin-down channel only shows a core pocket. More specifically, the spin-up Fermi surface shows two layers of peripheral pockets (the inner layer is shown in red) since the Fermi energy for the spin-up channel is lifted above the second valley band at the N point. This difference in Fermi surfaces, along with the differences in valence bands and DOS, indicates an unequal contribution of the two spin channels to the electronic properties, which may have profound implications for the thermoelectrics and spintronics of single crystalline samples [73,74,77,78]. Spin-polarized Fermi surfaces can be experimentally verified by spin-resolved angle-resolved photoemission spectroscopy or spin-resolved positron annihilation spectroscopy [91,92].

The total DOS curves for the bcc supercell structure and its 12.5% La-filled counterpart were further decomposed into partial DOS contributions from Co's p and d states, Sb's s and p states, and La's s and d states. Figure 5(a) shows the total and partial DOS for the bcc supercell. The peak corresponding to the VBM is negligible due to the quasilinear dispersion of the single valence band (cf. Fig. 3). The partial DOS analysis shows that the first valence DOS peak at -0.34 eV below the VBM consists of the hybridization from Co's d and Sb's p states, whereas the tiny conduction DOS peak corresponding to the CBM is dominated mainly by Co's d states, largely agreeing with the observations of Zhao *et al.* for the same bcc supercell [93]. Figure 5(b) shows the spin-polarized total and partial DOS for $La_{0.125}Co_4Sb_{12}$, where La's contribution is also presented. As shown, the two spins are nearly degenerate for the valence states but a large DOS offset exists for the conduction states. Again, only the spin-up channel shows significant DOS at the Fermi energy, which consists of a hybridization of Co's d states, Sb's s and p states, and the filler La's d states. The band structures and DOS of Co_4Sb_{12} and $La_{0.125}Co_4Sb_{12}$ constitute a vast contrast: the former material is an intrinsic semiconductor, while the latter is converted to a degenerate semiconductor. These results are in line with the electrical resistivity measurements of hot-pressed polycrystalline Co_4Sb_{12} and $La_{0.05}Co_4Sb_{12}$ samples by Nolas

et al. [45], and of the hot-pressed $La_{0.1}Co_4Sb_{12}$ sample by Mi *et al.* [44,47].

D. $La_{0.125}Co_4Sb_{11.875}$ and $La_{0.125}Co_4Sb_{11.750}$ with Sb vacancies

All of the above discussions concern only the electronic structures of $LaCo_{32}Sb_{96}$ (i.e., $La_{0.125}Co_4Sb_{12}$) without vacancy defects. However, Sb vacancies are easy to form during material synthesis due to the high vapor pressure of Sb. Especially, the formation of Sb vacancies is facilitated when the La content exceeds the FFL, in which case La and Sb form a secondary phase. In this subsection, we examine $LaCo_{32}Sb_{95}$ with a monovacancy defect (i.e., $La_{0.125}Co_4Sb_{11.875}$) and $LaCo_{32}Sb_{94}$ with a divacancy defect (i.e., $La_{0.125}Co_4Sb_{11.750}$). It should be noted that without La filling all Sb atoms in $CoSb_3$ are equivalent due to the $Im\bar{3}$ symmetry, leading to merely one type of monovacancy defect and two types of divacancy defects. However, once La is filled, the reduced crystal symmetry leads to a wide variety of nonequivalent Sb mono- and divacancy defects that in turn alter the electronic structures in different ways. For brevity, herein we study only six different scenarios for each by removing a Sb atom or a directly bonded Sb pair at six random locations, based on the previously optimized structure of $La_{0.125}Co_4Sb_{12}$. In the case of monovacancy defects, the structures optimized with spin polarization are more stable than those optimized without spin polarization by an average value of 30 meV per unit cell (Table S3, Supplemental Material [58]). In the case of divacancy defects, the structures optimized with spin polarization are more stable than those optimized without spin polarization by ∼1 (indicating near degeneracy) or 18 meV per unit cell, depending on the relative energies and total magnetizations (Table S3, Supplemental Material [58]). All of the optimized structures were used for static band structure calculations with the PBE functional.

Figure 6 compares the non-spin-polarized and spin-polarized band structures between $La_{0.125}Co_4Sb_{11.875}$ with a monovacancy defect and $La_{0.125}Co_4Sb_{11.750}$ with a divacancy defect. These results represent only the most stable one out of the six scenarios, respectively. Spin-polarized results for other scenarios of higher energies are presented in Figs. S2 and S3, Supplemental Material [58]. As shown in Fig. 6, the mono- and divacancy defects profoundly alter the band structure of the vacancy-free $La_{0.125}Co_4Sb_{12}$ [cf. Figs. 4(a) and 4(b)]. Particularly, the quasi-Dirac bands largely disappear while a number of vacancy-related defect bands emerge in the band gap region. These defect bands mainly result from the Sb atoms near the vacancy and, notably, they are of large dispersions. For $La_{0.125}Co_4Sb_{11.875}$, the Sb monovacancy defects induce electron deficiency that lowers the Fermi energy to the defect bands. Among the six band structures for the six defect scenarios, only one scenario is half-metallic [Fig. 6(a)], while the rest are semiconducting (Fig. S2). For $La_{0.125}Co_4Sb_{11.750}$, the band structures calculated for the six random divacancy scenarios indicate that all of them become conductors, as the Fermi energy is lowered more to cross the vacancy-derived bands in both spin channels [Figs. 6(b) and S3].

The electrical resistivity measurements of Nolas *et al.* using a hot-pressed polycrystalline $La_{0.23}Co_4Sb_{11.6}$ sample showed a degenerate semiconductor behavior [45]. From the band

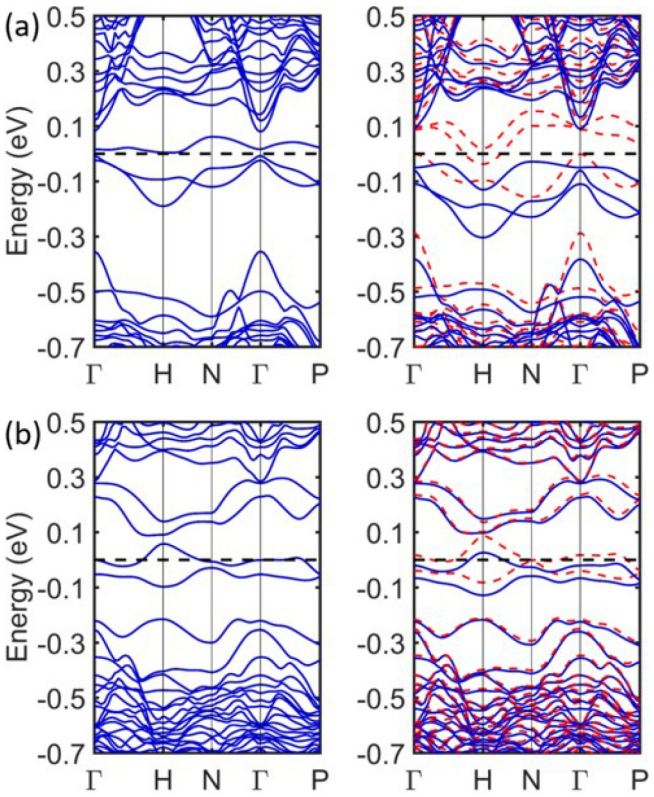

FIG. 6. (a) Non-spin-polarized (left) and spin-polarized (right) band structures of $LaCo_{32}Sb_{95}$ with a Sb monovacancy (i.e., $La_{0.125}Co_4Sb_{11.875}$) and (b) non-spin-polarized (left) and spin-polarized (right) band structures of $LaCo_{32}Sb_{94}$ with a Sb divacancy (i.e., $La_{0.125}Co_4Sb_{11.750}$). The Fermi energy is indicated by the horizontal dashed line.

structures of the six cases of $La_{0.125}Co_4Sb_{11.875}$, it appears that introducing a monovacancy defect does not promise a conductive behavior since the ratio of 1/6 for the half-metallic conductive grains in a polycrystalline sample could be too low to percolate charge carriers. However, the half-metallic structure is a lot more stable by ∼0.14 eV per unit cell than the rest of the structures studied (Table S3, Supplemental Material [58]), and therefore the synthesized $La_{0.125}Co_4Sb_{11.875}$ could have a half-metallic property as dictated by the large difference in stability. Since half metallicity is of great importance in the field of spintronics, these results suggest that $La_{0.125}Co_4Sb_{11.875}$ could be an excellent candidate material for experimental studies. For this purpose, a single crystal would be more appealing than polycrystalline samples in order to maintain the same spin polarization. In comparison, the bands of all six $La_{0.125}Co_4Sb_{11.750}$ structures with a divacancy defect suggest a conductive behavior without ambiguity. However, precaution should be taken when interpreting polycrystalline transport data because of the scattering of charge carriers at grain boundaries and at Sb vacancy defects. Note that the structures with mono- and divacancies examined here have fewer Sb vacancies as compared to the experimentally studied $La_{0.23}Co_4Sb_{11.6}$. Nonetheless, the results are still instructive regarding the effect of vacancies on the electronic structures of La-filled skutterudites.

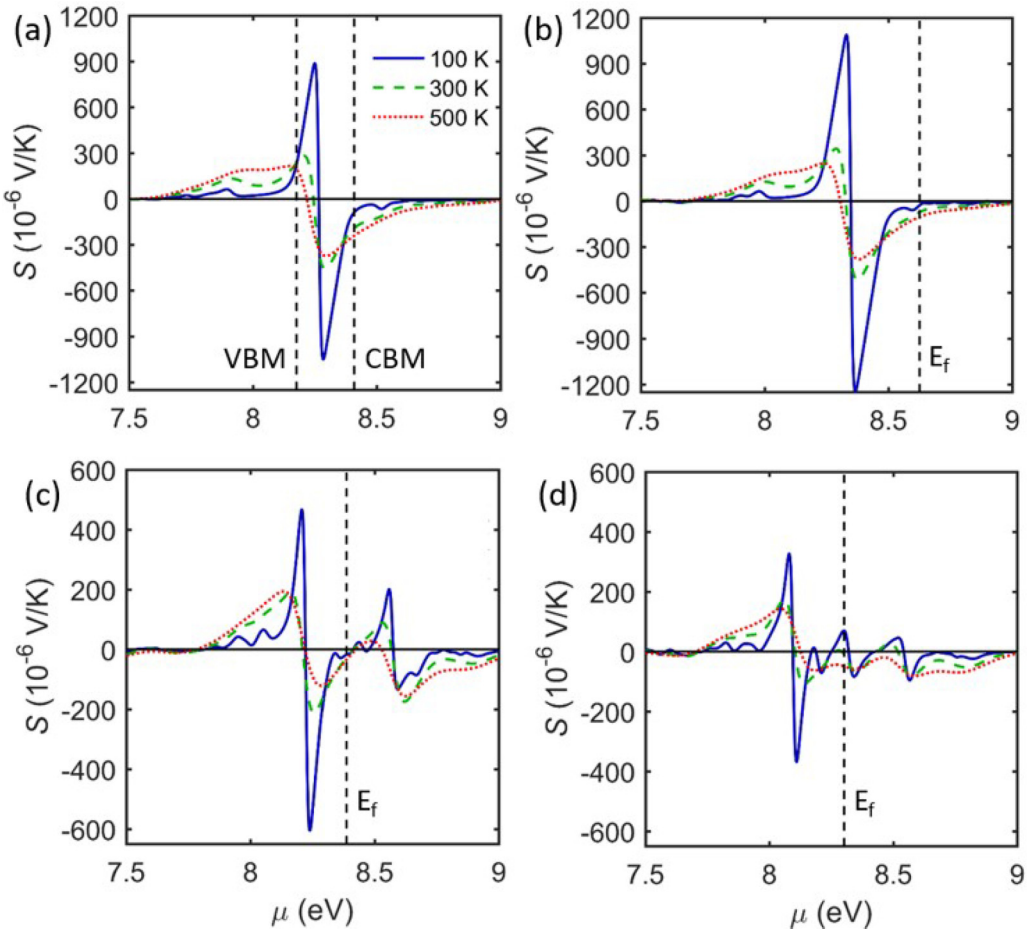

FIG. 7. Theoretical Seebeck coefficients S as a function of chemical potential μ for (a) Co_4Sb_{12}, (b) $La_{0.125}Co_4Sb_{12}$, (c) $La_{0.125}Co_4Sb_{11.875}$, and (d) $La_{0.125}Co_4Sb_{11.750}$ at different temperatures. Vertical dash lines denote the valence band minimum (VBM) and conduction band maximum (CBM) in (a), and the Fermi energy (E_f) at 0 K in (b)–(d).

E. Seebeck coefficients

Seebeck coefficients, S, are a transport parameter of utmost importance in thermoelectrics. In this subsection, we will compare the experimental Seebeck coefficients with our calculated results. Since our calculations are based on periodic boundary condition, applicable to single crystalline materials, whereas the experimental results were mostly obtained in polycrystalline samples, such a comparison warrants some justifications. First, pristine and La-filled $CoSb_3$ skutterudites adopt a cubic crystal structure, in which the Seebeck coefficients are isotropic. Moreover, grain boundary scattering affects the Seebeck coefficients, but the impact is typically small in coarse-grained materials. Finally, we adopt a Boltzmann transport model to calculate the Seebeck coefficients with a constant relaxation time approximation, in which the relaxation time can be regarded as a lump sum of various scattering mechanisms such as grain boundary, defect, and phonon scatterings.

Before comparing with experimental results, we examine the general trends in the Seebeck coefficients S directly calculated as a function of chemical potential μ. Figure 7 shows the calculated Seebeck coefficients at $T = 100, 300$, and 500 K for the four bcc supercell structures studied above, i.e., Co_4Sb_{12} (cf. Fig. 3), $La_{0.125}Co_4Sb_{12}$ (cf. Fig. 4), $La_{0.125}Co_4Sb_{11.875}$, and $La_{0.125}Co_4Sb_{11.750}$ (cf. Fig. 6). As a result of the spin-polarized electronic structures shown/discussed above, the electrical transport of the La-filled materials should be spin dependent. For simplicity, we first discuss the non-spin-dependent Seebeck coefficients. The spin-dependent results for the latter three are presented in Fig. S4, Supplemental Material [58]. The 500 K results are more relevant for practical midtemperature thermoelectric applications of $CoSb_3$-based skutterudites, while the 100 and 300 K results are also presented due to the experimentally studied temperature range for a few La-filled $CoSb_3$ skutterudites from 300 K down to 2–6 K [44,45].

As shown in Fig. 7(a), the Seebeck coefficients for the pristine Co_4Sb_{12} show two peaks sandwiched between the VBM and CBM, with the positive S peak closer to the VBM and the negative S peak midway between the VBM and CBM. The asymmetric peak locations are related to the different degeneracies between the frontier valence bands and conduction bands and their different DOS contributions (cf. Figs. 2 and 3). With P-type doping, the chemical potential shifts to the left, giving positive S values, whereas N-type doping causes a shift of chemical potential to the right, giving negative S values. In addition, with light P-type and N-type doping, the magnitude of S is found to decrease with increasing

T, as expected from a semiconductor. However, upon heavy P-type and N-type doping, the chemical potential can be shifted beyond the crossover point to give an inverted trend of increasing magnitude of S with increasing T, which is more like degenerate semiconductors or metals. These trends are consistent with the experimental data for lightly doped (10^{17} cm^{-3} for P-type and 10^{18} cm^{-3} for N-type) and heavily doped (10^{18}–10^{19} cm^{-3} for P-type and 10^{19}–10^{20} cm^{-3} for N-type) single crystalline $CoSb_3$ samples measured by Caillat *et al.* in the temperature range of 300–500 K [74].

Figures 7(b)–7(d) present the Seebeck coefficients of the three La-filled Co_4Sb_{12} with and without Sb vacancy defects. Compared to pristine $CoSb_3$, La filling raises the Fermi energy to higher chemical potentials. However, with increasing amount of defects, the Fermi energy is slightly shifted back to the left, in line with our understanding from the band structures shown above (cf. Fig. 6). For $La_{0.125}Co_4Sb_{12}$ without defects [Fig. 7(b)], the curves are in general similar to those of the pristine $CoSb_3$, as a result of the rigid band structure of pristine $CoSb_3$. Figure 7(b) also indicates that the Seebeck coefficients can be fine-tuned in the vicinity of the Fermi energy by the amount of La filling fraction, giving a smaller magnitude for a greater filling fraction. For $La_{0.125}Co_4Sb_{11.875}$ with a Sb monovacancy defect [Fig. 7(c)] and especially $La_{0.125}Co_4Sb_{11.750}$ with a Sb divacancy defect [Fig. 7(d)], the Seebeck coefficients exhibit some oscillations due to the presence of vacancy-related bands (cf. Fig. 6). As can be further seen in Figs. 7(b) and 7(c), the magnitude of S for the vacancy-free $La_{0.125}Co_4Sb_{12}$ and the $La_{0.125}Co_4Sb_{11.875}$ with a Sb monovacancy defect is predicted to increase with increasing T, implying heavy N-type doping. In contrast, the Seebeck coefficients of the $La_{0.125}Co_4Sb_{11.750}$ with a Sb divacancy defect may experience a change of sign in the vicinity of Fermi energy with increasing temperature due to the strong oscillation [Fig. 7(d)]. Note that these observations only represent general trends associated with the structures used for the calculations, especially in the cases with Sb vacancies. The actual Seebeck coefficients may be different depending on the locations of defects.

The spin-polarized Fermi surface as revealed above would naturally lead to spin-dependent Seebeck coefficients. In Fig. 8, we compare the non-spin-dependent and spin-dependent Seebeck coefficients of $La_{0.125}Co_4Sb_{12}$ as a function of temperature in the range of 0–300 K. Regardless of the spin polarization, all S curves exhibit degenerate semiconductor behavior in that the magnitude of S gradually increases with increasing temperature. To date, neither polycrystalline nor single crystalline $La_{0.125}Co_4Sb_{12}$ sample has been experimentally reported. Due to randomly spin-polarized grains and limited spin diffusion length in a polycrystalline sample, it is expected that the experimental Seebeck data of a polycrystalline $La_{0.125}Co_4Sb_{12}$ sample should be compared with the calculated non-spin-dependent Seebeck data. Meanwhile, the calculated spin-dependent Seebeck data are to be verified by the experimental data of a single crystalline $La_{0.125}Co_4Sb_{12}$ sample. As shown in Fig. 8, the non-spin-dependent S is sandwiched between the two spin-dependent curves. Notably, the magnitude of the spin-up S is smaller than that of the spin-down S, which can be understood in view of the Mott's relation $S \propto \partial \ln \mathrm{DOS}(E)/\partial E|_{E=E_f} = 1/\mathrm{DOS} \cdot \partial\, \mathrm{DOS}(E)/\partial E|_{E=E_f}$ [94].

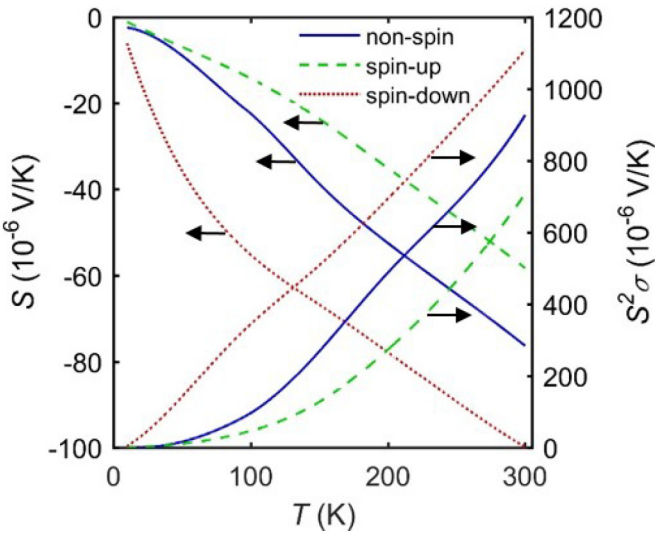

FIG. 8. Calculated non-spin-dependent and spin-dependent Seebeck coefficients S and power factor $S^2\sigma$ (where σ is electrical conductivity) of $La_{0.125}Co_4Sb_{12}$ as a function of temperature T based on its own electronic structure which intrinsically contains the information of carrier concentration.

In the present work, we have assumed a constant relaxation time, regardless of spin and energy; hence the difference between the spin-up and spin-down S curves is solely due to the difference in their spin-specific DOS near the Fermi energy [cf. Fig. 4(b)]. Figure 8 also shows non-spin-dependent and spin-dependent power factor $S^2\sigma$, where σ is electrical conductivity, as an illustration of spin-dependent thermoelectric properties [95,96]. These theoretically predicted spin-dependent thermoelectric properties invite further experimental studies of single crystalline $CoSb_3$ skutterudites with partial filling of La or other rare earth elements. Although it was found that the non-spin-polarized and spin-polarized solutions of La-filled $CoSb_3$ are nearly degenerate, it is possible that their energy difference may be enlarged by doping with other lanthanide fillers. Spin-dependent Seebeck coefficients may be possibly measured using spin valve devices [96], or via anomalous Nernst effects, etc. [97].

Next we compare the experimental Seebeck coefficients with our calculated results. Figure 9 shows the experimental Seebeck data S for P-type Co_4Sb_{12}, N-type $La_{0.05}Co_4Sb_{12}$, $La_{0.1}Co_4Sb_{12}$, and $La_{0.23}Co_4Sb_{11.6}$ skutterudites as a function of temperature T below 300 K digitized from the works of Mi *et al.* [44] and Nolas *et al.* [45]. Similar to the case of $La_{0.125}Co_4Sb_{12}$ shown above, all of these samples exhibit degenerate semiconductor behavior in that the magnitude of S gradually increases with increasing temperature, consistent with the relatively high carrier concentrations at 10^{18} cm^{-3} for the P-type sample and 10^{20}–10^{21} cm^{-3} for the partially La-filled N-type samples (Table I). For the partially La-filled samples without Sb vacancies, it is somewhat a surprise to see the magnitude of S for $La_{0.05}Co_4Sb_{12}$ to be very close to that of $La_{0.1}Co_4Sb_{12}$. In fact, the formula of the latter compound is merely a nominal ratio, whereas the actual La content was determined to be 0.049. Consequently, the two compounds are close in carrier concentration (Table I). In comparison, the

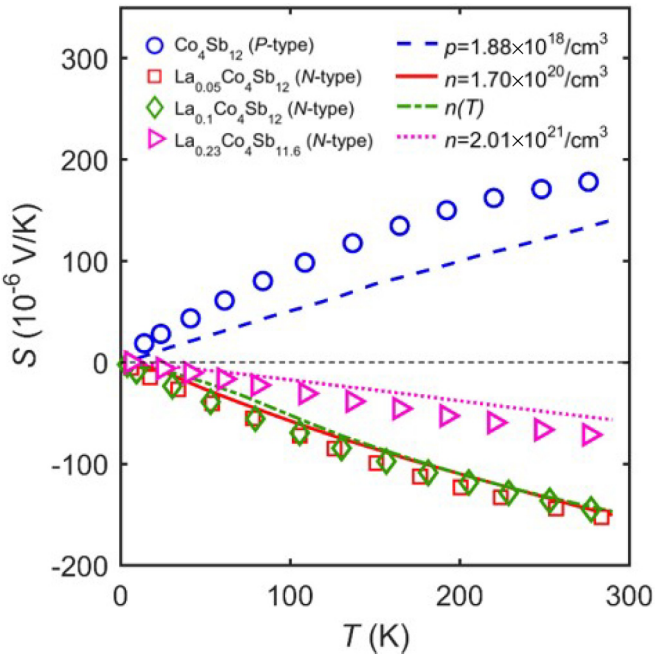

FIG. 9. Experimental Seebeck coefficients S as a function of temperature T for P-type and partially La-filled N-type Co_4Sb_{12} skutterudites (points) compared with the theoretical results (curves) calculated with the experimental carrier concentrations p or n for the four experimentally studied materials by using the host matrix's electronic structure based on the pristine Co_4Sb_{12}.

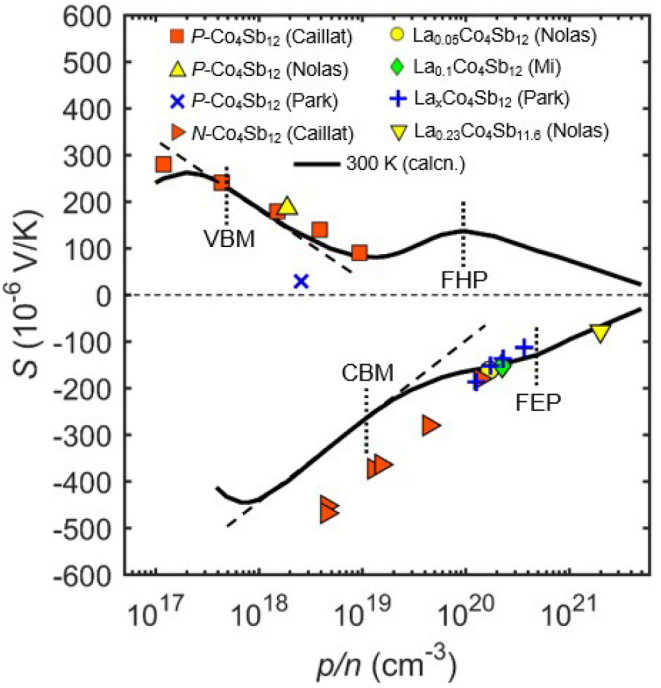

FIG. 10. Experimental Seebeck coefficients S at room temperature taken from Refs. [43–45,74], compared with calculated values at 300 K as a function of carrier concentration p for P-type and n for N-type Co_4Sb_{12} skutterudites. For $La_xCo_4Sb_{12}$ with nominal filling fraction of $x = 0.1$–0.4, the carrier concentrations were obtained at room temperature while the Seebeck coefficients were obtained at 320 K. The vertical dotted line segments indicate the carrier concentrations that are required to shift the Fermi energy to the valence band maximum (VBM), conduction band minimum (CBM), Fermi hole pocket (FHP), and Fermi electron pocket (FEP). Dashed lines along the linear section of the theoretical curves are provided to guide the eye.

magnitude of S is significantly reduced for $La_{0.23}Co_4Sb_{11.6}$, due to its much higher La filling and the presence of Sb vacancies.

Figure 9 also presents the calculated Seebeck coefficients $S(T)$ in the same temperature range. The experimental La-filling fractions and Sb vacancy ratios are rarely commensurate with $(1/2)^n$ ($n = 0,1,2,3,\ldots$), and yet due to the adoption of supercells, the calculations of electronic properties and Seebeck coefficients are restricted to a La-filling fraction or Sb vacancy ratio of $(1/2)^n$, as illustrated above for $La_{0.125}Co_4Sb_{12}$ (Fig. 8). To facilitate the comparison with the four experimentally studied incommensurate materials, herein we adopted a different approach by using the electronic structure of the host matrix based on the pristine bcc primitive cell Co_4Sb_{12} along with their respective experimentally measured carrier concentrations (Table I). The calculations were done using a semiclassical Boltzmann transport model based on a temperature-independent carrier concentration (except $La_{0.1}Co_4Sb_{12}$), a constant relaxation time of carriers, and no contribution from minority carriers. Despite these approximations, Fig. 9 shows a fairly satisfactory agreement with the experimental data, especially for $La_{0.05}Co_4Sb_{12}$ and $La_{0.1}Co_4Sb_{12}$. The agreement is reasonable because the partial La filling largely serves to raise the Fermi energy without significantly changing the rigid band structure of the host matrix. However, this is not the case for $La_{0.23}Co_4Sb_{11.6}$, which contains Sb vacancies in addition to the high La filling. Consequently, the electronic structure of the host matrix has been changed. Similarly, the rather large discrepancy in the case of P-type Co_4Sb_{12} could be ascribed to the stoichiometric changes or structural defects associated with the growth technique employed [74].

Finally, we examine the Seebeck coefficient as a function of carrier concentration p and n for both P- and N-type $CoSb_3$ skutterudites (Fig. 10). The carrier concentration governs the electrical transport properties of a semiconductor, including the Seebeck coefficient. In the simplest case of a degenerate single parabolic band with electron-acoustic phonon scattering, $S = 8m^*\pi^2 {k_B}^2/(3qh^2T)[\pi/(3\rho)]^{2/3}$, where k_B is the Boltzmann constant, q is carrier charge ($+e$ or $-e$ for P- or N-type materials, respectively), h is the Planck constant, m^* is band effective mass, and ρ is carrier concentration (p or n for P- or N-type materials, respectively). This implies the existence of a linear dependence between S and $\log(\rho)$ [98,99], usually called the Pisarenko plot [100]. Notwithstanding it is based on a degenerate single parabolic band, as a result of the complex band structure and scattering mechanism of $CoSb_3$, we still observe in Fig. 10 a linearity between S and $\log(p)$ at p of $\sim 10^{17}$–10^{19} cm^{-3} for the P-type samples, and between S and $\log(n)$ at n of $\sim 10^{18}$–10^{20} cm^{-3} for the N-type samples. At higher carrier concentrations side, the calculated data exhibit a deviation from the quasilinear dependence of S vs $\log(p)$ or $\log(n)$ by showing a hump. Based on the band structure

of $CoSb_3$ [cf. Fig. 2(a)], this feature arises from the highly degenerate electron and hole pockets on the Fermi surface deep in the valence and conduction bands.

As shown in Fig. 10, the calculated Seebeck coefficients are about 50 μV/K lower than the experimental data of *P*-type $CoSb_3$ skutterudite samples (see also Fig. 9). In comparison, the match between the calculated Seebeck coefficients and the experimental data of *N*-type samples is only good above the carrier concentration of $10^{20}\,cm^{-3}$, below which the experimental and calculated data follow the same temperature dependence but the calculated results are systematically lower than the experimental data. In light of the well-known underestimation of the band gap by DFT, we tested the effect of a scissor operator Δ by increasing the band gap to the GW value of 0.34 eV [70]. In addition, the effect of SOC on the Seebeck coefficient is also examined. As shown in Fig. S5, Supplemental Material, neither of these corrections gives a significant improvement [58]. Therefore, the persistent discrepancies may have partially resulted from the adoption of the host matrix's electronic structure for Seebeck coefficient calculations. The rigid band approximation may be violated by the structural changes of the host matrix. Taking the Caillat data for instance [74], the *P*-type Co_4Sb_{12} samples suffer from stoichiometric changes or structural defects as a result of the growth technique employed, while the *N*-type Co_4Sb_{12} samples were obtained by substitution of Sb with Te or Pd that may also change the crystal structure and electronic properties. In addition, the discrepancies, especially for the *N*-type materials, may be also associated with the fact that *N*-type doping involves the virtual conduction bands, which are challenging to capture correctly. Furthermore, the Seebeck coefficients were calculated based on the ground-state electronic structures, whereas the thermoelectric transport is an excited-state phenomenon. We speculate that GW-based calculations may be exploited in the future to improve the agreement with experimental results.

IV. CONCLUSIONS

Using *ab initio* DFT along with semiclassical Boltzmann transport theory, we have systematically studied the electronic and thermoelectric properties of pristine and La-filled $CoSb_3$ with and without Sb's mono- and divacancy defects. The electronic structure of pristine $CoSb_3$ can be interpreted as having several kinds of band gaps, and therefore it is imperative to differentiate which of the different types of band gaps is being referred to when making comparisons between theoretical calculations and experimental results. Partial La filling largely serves to raise the Fermi energy to a position slightly above the degenerate valley bands. Sb vacancies introduce dispersive bands in the band gap region and lower the Fermi energy to the vacancy-derived bands. The peculiar quasi-Dirac band in the pristine $CoSb_3$ largely survives the La filling but not the Sb vacancies. Interestingly, introducing monovacancy defects may lead to a half-metallic electronic property that is of great importance in the field of spintronics. Seebeck coefficients have been calculated for materials with incommensurate La filling fractions and/or Sb vacancy ratios indirectly using the experimental carrier concentrations p/n along with the host matrix's density of states. In comparison, for materials with commensurate La filling fractions and/or Sb vacancy ratios, we have demonstrated that Seebeck coefficients can be calculated directly from their own density of states which already contain the intrinsic information for p/n. Seebeck coefficients calculated as a function of p/n corroborate a thermoelectrically favorable role at high filling fractions played by the electron/hole pockets on the Fermi surface associated with the degenerate valleys/hills in the conduction/valence bands, respectively.

We have shown that the non-spin-polarized and spin-polarized solutions of La-filled $CoSb_3$ are nearly degenerate. However, the band structure, density of states, and Fermi surface of the latter are significantly spin polarized. The spin polarization naturally gives rise to spin-dependent Seebeck coefficients and power factors, indicating an unequal contribution of two spin channels to the electronic and thermoelectric properties, which may have profound implications for the thermoelectrics and spintronics of single crystalline samples. These theoretically predicted spin-dependent results invite further experimental studies of single crystalline $CoSb_3$ skutterudites with partial La filling or other rare earth elements. Experimental methods for the measurements of spin-polarized Fermi surfaces and spin-dependent thermoelectric properties have been suggested. On the other hand, due to randomly spin-polarized grains and limited spin diffusion length, the experimental thermoelectric properties of polycrystalline samples should be compared with non-spin-polarized calculation results. We note that the energy difference between the spin-polarized and the non-spin-polarized solutions is very small and it may depend on the exchange correlation functionals or pseudopotentials used for the calculations. However, the energy difference may be enlarged by doping with other lanthanide fillers, and therefore the spin-dependent properties we presented for La-filled $CoSb_3$ are still enlightening.

Over the past decades, $CoSb_3$ skutterudite has received extensive theoretical and experimental studies. Nonetheless, there is a conspicuous knowledge gap concerning the impact of La filler atoms, Sb vacancies, and their interplay on the electronic and thermoelectric properties of $CoSb_3$. Our theoretical studies presented herein have discussed previously reported experimental results, including band gaps, electrical conductions, and Seebeck coefficients. More importantly, the results are instrumental in helping elucidate the causality link between electronic structures and thermoelectric transport properties. While the present work was initially motivated by the thermoelectrics of some experimentally studied *N*-type La-filled $CoSb_3$, the model systems studied have a too limited phase space in terms of La filling fractions and Sb vacancies to exhaustively explore the potential of this class of materials for thermoelectric applications. Practically, the multiple filling approach has been shown to be more effective in enhancing the midtemperature thermoelectric performance. Nonetheless, the fundamental investigations may lay the groundwork for future studies of other lanthanides containing f electrons. The understanding of spin-polarized Fermi surfaces, spin-dependent thermoelectric properties, and half-metallic electronic structures as revealed in this work also hints at the possible spintronic applications of $CoSb_3$ skutterudite.

ACKNOWLEDGMENTS

This research was conducted at the Center for Nanophase Materials Sciences (CNMS) of Oak Ridge National Laboratory, which is a U.S. Department of Energy (DOE) Office of Science User Facility. The work also utilized computational resources of the National Energy Research Scientific Computing Center (NERSC), which are supported by the Office of Science of the U.S. DOE under Contract No. DE-AC02-05CH11231. C.H., Y.F.L., M.H.Z., and J.H. would like to acknowledge the support of National Science Foundation Grant No. DMR 1307740. The authors thank Dr. Peter Doak of CNMS for comments and suggestions.

[1] S. Chu and A. Majumdar, Nature (London) **488**, 294 (2012).
[2] G. J. Snyder and E. S. Toberer, Nat. Mater. **7**, 105 (2008).
[3] G. S. Nolas, D. T. Morelli, and T. M. Tritt, Annu. Rev. Mater. Sci. **29**, 89 (1999).
[4] C. Uher, Semicond. Semimet. **69**, 139 (2001).
[5] C. Sekine, T. Uchiumi, I. Shirotani, and T. Yagi, Phys. Rev. Lett. **79**, 3218 (1997).
[6] C. Lee, H. Matsuhata, A. Yamamoto, T. Ohta, H. Takazawa, K. Ueno, C. Sekine, I. Shirotani, and T. Hirayama, J. Phys.: Condens. Matter **13**, 45 (2001).
[7] K. Hachitani, H. Fukazawa, Y. Kohori, I. Watanabe, C. Sekine, and I. Shirotani, Phys. Rev. B **73**, 052408 (2006).
[8] M. Kohgi *et al.*, J. Phys. Soc. Jpn. **72**, 1002 (2003).
[9] H. Kotegawa, M. Yogi, Y. Imamura, Y. Kawasaki, G.-q. Zheng, Y. Kitaoka, S. Ohsaki, H. Sugawara, Y. Aoki, and H. Sato, Phys. Rev. Lett. **90**, 027001 (2003).
[10] E. D. Bauer, N. A. Frederick, P. C. Ho, V. S. Zapf, and M. B. Maple, Phys. Rev. B **65**, 100506 (2002).
[11] Y. Aoki, T. Namiki, T. D. Matsuda, K. Abe, H. Sugawara, and H. Sato, Phys. Rev. B **65**, 064446 (2002).
[12] N. Takeda and M. Ishikawa, J. Phys.: Condens. Matter **13**, 5971 (2001).
[13] M. Nicklas, S. Kirchner, R. Borth, R. Gumeniuk, W. Schnelle, H. Rosner, H. Borrmann, A. Leithe-Jasper, Y. Grin, and F. Steglich, Phys. Rev. Lett. **109**, 236405 (2012).
[14] R. E. Baumbach, P. C. Ho, T. A. Sayles, M. B. Maple, R. Wawryk, T. Cichorek, A. Pietraszko, and Z. Henkie, Proc. Natl. Acad. Sci. USA **105**, 17307 (2008).
[15] P. Puneet, J. He, S. Zhu, and T. M. Tritt, J. Appl. Phys. **112**, 033710 (2012).
[16] R. T. M. Dobbe, W. J. Lustenhouwer, M. A. Zakrzewski, K. Goubitz, J. Fraanje, and H. Schenk, Can. Mineral. **32**, 179 (1994).
[17] Z. G. Mei, J. Yang, Y. Z. Pei, W. Zhang, L. D. Chen, and J. H. Yang, Phys. Rev. B **77**, 045202 (2008).
[18] L. D. Chen, T. Kawahara, X. F. Tang, T. Goto, T. Hirai, J. S. Dyck, W. Chen, and C. Uher, J. Appl. Phys. **90**, 1864 (2001).
[19] J. Yang, L. Zhang, Y. Liu, C. Chen, J. Li, D. Yu, J. He, Z. Liu, Y. Tian, and B. Xu, J. Appl. Phys. **113**, 113703 (2013).
[20] X. Shi, W. Zhang, L. D. Chen, J. Yang, and C. Uher, Acta Mater. **56**, 1733 (2008).
[21] Y. Li, P. Qiu, H. Duan, J. Chen, G. J. Snyder, X. Shi, B. B. Iversen, and L. Chen, J. Mater. Chem. C **4**, 4374 (2016).
[22] S. Katsuyama, Y. Shichijo, M. Ito, K. Majima, and H. Nagai, J. Appl. Phys. **84**, 6708 (1998).
[23] J. W. Sharp, E. C. Jones, R. K. Williams, P. M. Martin, and B. C. Sales, J. Appl. Phys. **78**, 1013 (1995).
[24] B. C. Sales, D. Mandrus, and R. K. Williams, Science **272**, 1325 (1996).
[25] D. T. Morelli, G. P. Meisner, B. Chen, S. Hu, and C. Uher, Phys. Rev. B **56**, 7376 (1997).
[26] G. A. Lamberton, Jr., R. H. Tedstrom, T. M. Tritt, and G. S. Nolas, J. Appl. Phys. **97**, 113715 (2005).
[27] D. J. Singh and M.–H. Du, Phys. Rev. B **82**, 075115 (2010).
[28] G. Xing, X. Fan, W. Zheng, Y. Ma, H. Shi, and D. Singh, Sci. Rep. **5**, 10782 (2015).
[29] H. Luo, J. W. Krizan, L. Muechler, N. Haldolaarachchige, T. Klimczuk, W. Xie, M. K. Fuccillo, C. Felser, and R. J. Cava, Nat. Commun. **6**, 6489 (2015).
[30] G. A. Slack, in *Handbook of Thermoelectrics*, edited by D. M. Rowe (CRC Press, Boca Raton, FL, 1995), Chap. 34, Sec. D, p. 407.
[31] G. S. Nolas, G. A. Slack, D. T. Morelli, T. M. Tritt, and A. C. Ehrlich, J. Appl. Phys. **79**, 4002 (1996).
[32] B. C. Sales, D. Mandrus, B. C. Chakoumakos, V. Keppens, and J. R. Thompson, Phys. Rev. B **56**, 15081 (1997).
[33] X.-Q. Yang, P.-C. Zhai, L.-S. Liu, and Q.-J. Zhang, Phys. B: Condens. Matter **407**, 2234 (2012).
[34] Y. Tang, R. Hanus, S.-W. Chen, and G. J. Snyder, Nat. Commun. **6**, 7584 (2015).
[35] G. Tan, Y. Zheng, and X. Tang, Appl. Phys. Lett. **103**, 183904 (2013).
[36] W. J. Graff, X. Zeng, M. A. Dehkordi, J. He, and T. M. Tritt, J. Mater. Chem. A **2**, 8933 (2014).
[37] G. A. Lamberton, Jr., S. Bhattacharya, R. T. Littleton, M. A. Kaeser, R. H. Tedstrom, T. M. Tritt, J. Yang, and G. S. Nolas, Appl. Phys. Lett. **80**, 598 (2002).
[38] Y. Tang, S. Chen, and G. J. Snyder, J. Materiomics **1**, 75 (2015).
[39] S. Wang, J. Salvador, J. Yang, P. Wei, B. Duan, and J. Yang, NPG Asia Mater. **8**, e285 (2016).
[40] G. S. Nolas, M. Kaeser, R. T. Littleton IV, and T. M. Tritt, Appl. Phys. Lett. **77**, 1855 (2000).
[41] X. Shi, J. Yang, J. Salvador, M. Chi, J. Cho, H. Wang, S. Bai, J. Yang, W. Zhang, and L. Chen, J. Am. Chem. Soc. **133**, 7837 (2011).
[42] G. Rogl, A. Grytsiv, P. Rogl, N. Peranio, E. Bauer, M. Zehetbauer, and O. Eibl, Acta Mater. **63**, 30 (2014).
[43] K. Park, S. Lee, W. Seo, S. Baek, D. Shin, and I. Kim, J. Korean Phys. Soc. **64**, 1004 (2014).
[44] J.-L. Mi, M. Christensen, E. Nishibori, and B. B. Iversen, Phys. Rev. B **84**, 064114 (2011).
[45] G. S. Nolas, J. L. Cohn, and G. A. Slack, Phys. Rev. B **58**, 164 (1998).
[46] X. Shi, W. Zhang, L. D. Chen, and J. Yang, Phys. Rev. Lett. **95**, 185503 (2005).

[47] J.-L. Mi, M. Christensen, E. Nishibori, V. Kuznetsov, D. M. Rowe, and B. B. Iversen. J. Appl. Phys. **107**, 113507 (2011).

[48] K. Koga, K. Akai, K. Oshiro, and M. Matsuura, in *Proceedings of the 20th International Conference on Thermoelectrics* (ICT, Beijing, 2001), p.105.

[49] A. Zhou, L.-S. Liu, P.-C. Zhai, W.-Y. Zhao, and Q.-J. Zhang, J. Electron. Mater. **39**, 1832 (2010).

[50] G. Kresse and J. Hafner, Phys. Rev. B **47**, 558 (1993).

[51] G. Kresse and J. Furthmüller, Phys. Rev. B **54**, 11169 (1996).

[52] P. E. Blöchl, Phys. Rev. B **50**, 17953 (1994).

[53] G. Kresse and D. Joubert, Phys. Rev. B **59**, 1758 (1999).

[54] Y.-H. Tian, J. Huang, X. Sheng, B. G. Sumpter, M. Yoon, and M. Kertesz, Nano Lett. **15**, 5482 (2015).

[55] S. Lebegue, J. Harl, T. Gould, J. G. Angyan, G. Kresse, and J. F. Dobson, Phys. Rev. Lett. **105**, 196401 (2010).

[56] J. Zhou, J. Huang, B. G. Sumpter, P. R. C. Kent, H. Terrones, and S. C. Smith, J. Phys. Chem. C **117**, 25817 (2013).

[57] T. Bucko, S. Lebegue, J. Hafner, and J. G. Angyan, Phys. Rev. B **87**, 064110 (2013).

[58] See Supplemental Material at http://link.aps.org/supplemental/10.1103/PhysRevB.95.165204 for the structural data of seventeen cif files of $CoSb_3$ from ICSD; structural optimizations calculated by a gamut of exchange-correlation functionals with and without vdW corrections compared with a representative experimental structure; total energies and magnetizations for La-filled $CoSb_3$ skutterudites with and without Sb vacancy defects; convergence studies of the spin-polarized and non-spin-polarized solutions for La-filled $CoSb_3$; rigid scan of potential energy surfaces as a function of the displacement of La filler atom from the dodecahedron cage center along five representative paths; spin-polarized band structures of $La_{0.125}Co_4Sb_{11.875}$ and $La_{0.125}Co_4Sb_{11.750}$; spin-up and spin-down Seebeck coefficients of $La_{0.125}Co_4Sb_{12}$, $La_{0.125}Co_4Sb_{11.875}$, and $La_{0.125}Co_4Sb_{11.750}$; Seebeck coefficients at 300 K calculated using PBE alone, PBE plus a scissor operator, and PBE plus SOC as a function of carrier concentrations.

[59] J. Klimeš, D. R. Bowler, and A. Michelides, J. Phys.: Condens. Matter **22**, 022201 (2010).

[60] J. P. Perdew, K. Burke, and M. Ernzerhof, Phys. Rev. Lett. **77**, 3865 (1996).

[61] D. J. Singh and W. E. Pickett, Phys. Rev. B **50**, 11235 (1994).

[62] S. Ram, V. Kanchana, and M. C. Valsakumar, J. Appl. Phys. **115**, 093903 (2014).

[63] A. A. Mostofi, J. R. Yates, Y.-S. Lee, I. Souza, D. Vanderbilt, and N. Marzari, Comput. Phys. Commun. **178**, 685 (2008).

[64] A. Kokalj, Comput. Mater. Sci. **28**, 155 (2003).

[65] G. Pizzi, D. Volja, B. Kozinsky, M. Fornari, and N. Marzari, Comput. Phys. Commun. **185**, 422 (2014).

[66] D. Wee, B. Kozinsky, N. Marzari, and M. Fornari, Phys. Rev. B **81**, 045204 (2010).

[67] J. O. Sofo and G. D. Mahan, Phys. Rev. B **58**, 15620 (1998).

[68] I. Lefebvre-Devos, M. Lassalle, X. Wallart, J. Olivier-Fourcade, L. Monconduit, and J. C. Jumas, Phys. Rev. B **63**, 125110 (2001).

[69] L. Hammerschmidt, S. Schlecht, and B. Paulus, Phys. Status Solidi A **210**, 131 (2013).

[70] B. Khan, H. A. R. Saifullah, S. Jalali-Asadabadi, I. Khan, and I. Ahmad, J. Alloys Compd. **647**, 364 (2015).

[71] F. Tran and P. Blaha, Phys. Rev. Lett. **102**, 226401 (2009).

[72] D. Koller, F. Tran, and P. Blaha, Phys. Rev. B **85**, 155109 (2012).

[73] G. S. Nolas, G. A. Slack, T. Caillat, and G. P. Meisner, J. Appl. Phys. **79**, 2622 (1996).

[74] T. Caillat, A. Borshchevsky, and J. P. Fleurial, J. Appl. Phys. **80**, 4442 (1996).

[75] L. D. Dudkin and N. Kh. Abrikosov, Sov. Phys. Solid State **1**, 126 (1959).

[76] K. Matsubara, T. Iyanaga, T. Tsubouchi, K. Kishimoto, and T. Koyanagi, in Proceedings of Thirteenth International Conference on Thermoelectrics, edited by B. Mathiprakasm and P. Heenan, AIP Conf. Proc. No. 316 (AIP, New York, 1995), p. 226.

[77] D. Mandrus, A. Migliori, T. W. Darling, M. F. Hundley, E. J. Peterson, and J. D. Thompson, Phys. Rev. B **52**, 4926 (1995).

[78] E. Arushanov, M. Respaud, H. Rakoto, J. M. Broto, and T. Caillat, Phys. Rev. B **61**, 4672 (2000).

[79] J. Nagao, M. Ferhat, H. Anno, K. Matsubara, E. Hatta, and K. Mukasa, Appl. Phys. Lett. **76**, 3436 (2000).

[80] J. C. Smith, S. Banerjee, V. Pardo, and W. E. Pickett, Phys. Rev. Lett. **106**, 056401 (2011).

[81] A. H. C. Neto, F. Guinea, N. M. R. Peres, K. S. Novoselov, and A. K. Geim, Rev. Mod. Phys. **81**, 109 (2009).

[82] M. Neupane *et al.*, Nat. Commun. **5**, 3786 (2014).

[83] Z. K. Liu *et al.*, Science **343**, 864 (2014).

[84] S.-Y. Xu *et al.*, Science **349**, 613 (2015).

[85] Y. Tang, Z. M. Gibbs, L. A. Agapito, G. Li, H. Kim, M. B. Nardelli, S. Curtarolo, and G. J. Snyder, Nat. Mater. **14**, 1223 (2015).

[86] Y. Pei, X. Shi, A. LaLonde, H. Wang, L. Chen, and G. J. Snyder, Nature (London) **473**, 66 (2011).

[87] Y. Tang, Y. Qiu, L. Xi, X. Shi, W. Zhang, L. Chen, S. Tseng, S.-W. Chen, and G. J. Snyder, Energy Environ. Sci. **7**, 812 (2014).

[88] D. J. Singh, in *Proceedings of 5th International Conference on Solid-State and Integrated Circuit Technology* (IEEE, Beijing, 1998), p. 856.

[89] W.-Z. Cai, L.-M. Wu, L.-H. Li, and L. Chen, Eur. J. Inorg. Chem. **2009**, 230 (2009).

[90] L. Hammerschmidt, M. Quennet, K. Topfer, and B. Paulus, Surf. Sci. **637–638**, 124 (2015).

[91] P. D. Johnson, Rep. Prog. Phys. **60**, 1217 (1997).

[92] A. Kawasuso, Y. Fukaya, M. Maekawa, I. Mochizuki, and H. Zhang, J. Phys.: Conf. Ser. **443**, 012084 (2013).

[93] W. Zhao *et al.*, Nat. Commun. **6**, 6197 (2015).

[94] M. Cutler and N. F. Mott, Phys. Rev. **181**, 1136 (1969).

[95] I. Campbell and A. Fert, in *Handbook of Ferromagnetic Materials*, edited by E. P. Wohlfarth (Elsevier, North-Holland, 1982), Vol. 3, Chap. 9, p. 747.

[96] F. K. Dejene, J. Flipse, and B. J. van Wees, Phys. Rev. B **86**, 024436 (2012).

[97] H. Wu, C. H. Wan, Z. H. Yuan, X. Zhang, J. Jiang, Q. T. Zhang, Z. C. Wen, and X. F. Han, Phys. Rev. B **92**, 054404 (2015).

[98] T. Katase, K. Endo, and H. Ohta, Phys. Rev. B **90**, 161105 (2014).

[99] G. H. Jonker, Philips Res. Rep. **23**, 131 (1968).

[100] A. F. Ioffe, *Physics of Semiconductors* (Academic, New York, 1960).